Developing a 3-D, lumped-mass model to present behaviour of large deformation surface based continuum robots

Hossein Habibi[1], Rongjie Kang[2], Ian D. Walker[3], Isuru S. Godage[4] and David T. Branson[5]

[1] School of Science, Engineering and Design, Teesside University, Middlesbrough TS1 3BX, UK, H.Habibi@tees.ac.uk.

[2] Key Laboratory of Mechanism Theory and Equipment Design of Ministry of Education, School of Mechanical Engineering, Tianjin University, Tianjin, China, rjkang@tju.edu.cn.

[3] Department of Electrical & Computer Engineering, Clemson University, Clemson, SC 29634-0915, US, iwalker@clemson.edu.

[4] School of Computing, DePaul University, Chicago, IL 60604, igodage@depaul.edu.

[5] Advanced Manufacturing Technology Research Group, Faculty of Engineering, University of Nottingham, Nottingham, UK, David.Branson@nottingham.ac.uk.

Abstract. The deployment of continuum robotic surfaces has strong potential over a wide range of engineering disciplines. To allow such compliant, actively actuated surfaces to be controlled accurately and efficiently, reliable kinematic and dynamic models are required. The main challenge appears when the continuum surfaces become very flexible and undergo large deformations, an issue which is little studied in continuum robotics to date. This paper tackles this problem through the application of a lumped-mass approach for analysis of continuum surfaces that are subject to large deformations due to either gravity or external loading applied by representative flexible actuators. The developed model describes the surface kinematics by providing a means of solving for the displacement profile across the surface. The model takes into account all the essential factors such as gravitational effects, material properties of a flexible plate, inertial forces, material damping, and in-depth shear effects across the surface. An experimental setup has been developed to test an actuated flexible surface under different boundary conditions, with results showing mean percentage error of 4.8% at measured surface points.

Keywords: Large Deformation Continuum Surfaces, Soft Robotics, Lumped-Mass Modelling.

1 Introduction

Surfaces capable of large deformations are progressively being considered to improve performance across a wide range of engineering applications. This can range from manufacturing processes such as composites formation or devising nature-inspired surface-like robots. Such flexible surfaces undergoing large deformations could also be used in airplane body structures to achieve better aerodynamic lift control, or used in vehicles to reduce drag. In terms of healthcare such soft systems are already in use [1] with controlled surfaces for use as exoskeletons under development by multiple research groups.

To employ such Large Displacement Continuum Surfaces (LDCS) efficiently, they need to be well adapted to the use of smart, controlled actuation that deforms the surfaces into an accurate, desired profile. In fact, the surface can be considered as a novel end-effector of a

control system which is viewed and analysed within the area of continuum robotics. Fig. 1 depicts a schematic LDCS deformed into multiple curvatures by means of actuation elements mounted on the surface edges.

In the area of continuum robotics, arms and manipulators have been well studied. Examples can be found in [2], [3], [4], [5], [6], [7], [8], and [9] where most of these are achieved through nature-inspired motion to be utilised for different tasks in industry, healthcare, manufacturing, or environments. However, unlike the relatively prolific number of studies on arm based structures, the research on LDCS within the continuum robotics area is relatively limited where to date LDCS have largely operated in 'open loop' with the placement and control of actuation elements based mainly on user intuition and experience. So far there is limited work attempting to provide models for such actuated continuum surfaces to enable model based control and simulation. This results in largely 'trial and error' based methods in their design and control that increases production costs and reduces performance. To remove this problem an adaptive and efficient dynamic model needs to be developed to readily characterize fairly precise positions incorporating interactive forces applied by actuators and external force elements. This will enable surfaces to be accurately simulated and the resulting model made available for model based control methods.

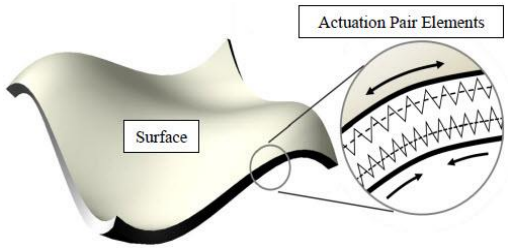

Fig. 1. Schematic diagram of a large deformation continuum surfaces (LDCS). Actuation elements in this case are placed along the edge, resulting in localized curvature through antagonistic actions.

Kano et al [10] developed the model of a two-dimensional sheet-like robot. Inspired by the decentralized control scheme of the scaffold-based locomotion of snakes, the surface undergoes large bends but it lacks information on the quality and quantity of induced curvatures and varying profiles. Medina et al. developed an actuated continuum surface using a shape memory alloy (SMA) material grid and further developed a model using Euler-Lagrange methods [11]. However, the array has poor scalability, as to improve performance and surface size the number of wires and nodes would be increased, resulting in dramatically increased computational demand. Also, SMA wires can withstand relatively small external forces, and are therefore, unable to be used for applications that require significant force interactions with the surface. Another approach is the use of the *phantom muscle method* by Merino et al [12] to present a kinematic model for LDCSs using an infinite number of interpolated curves parallel to the single actuator when deformed by this actuator. This mathematical model is not computationally demanding, but it lacks to account for material properties, gravitational effects etc. The work presented here gives the development of a generalized LDCS model using a lumped-mass approach to model dynamic effects such as including gravitational loading, compliance, and the material

properties etc. In addition, the model takes in-depth bending shear effects into account for thick plates undergoing large deformations through its specific two-layer configuration that has not been done or considered in previous studies by lumped-mass approaches.

In Section II, the principles of formulation, assumptions, and relevant equations of the dynamical surface model using the lumped-mass approach is introduced. Section 3 details the experimental setup and validation technique under gravity. Section 4, compares and discusses the modelling and experimental results on the performance of the surface for two different boundary conditions. Finally, concluding remarks and future work to be carried out to enhance or promote the current development are provided in Section 5.

2 Lumped-mass approach to model LDCS

This section explains the development of the surface model, which uses a lumped-mass approach. This modelling strategy has been extensively used for its consistency with large deformations, ease of implementation, avoidance of treating rigid and flexible motion in different ways, and its claim to represent in a generic way a range of systems of importance in engineering [13], [14], and [15]. The work accomplished via this technique also exploits its considerable computational efficiency along with the reliable capture of system dynamics through low-order lumped models, e.g. [16] and [17]. The modes of interest of, e.g., a flexible beam, can be modelled with a small number of undeformable masses, interconnected by springs and dampers [17]. For example, Kino et al. [18] and Torfs et al., [19] discretized a beam with a number of masses equal to the number of modes. The models predict very well the behaviour of the flexible beam and are well suited for controller design. However, the division of the beam into masses and the determination of the spring and damper constants is rather intuitive and empirical.

In this technique, lumped masses are linked together via linear springs and dampers. Each node/dot of the grid can be then subjected to its own weight, damping effects, and the reaction spring forces by the surrounding masses. Hence the momentum forces are transmitted to each mass due to the motion of neighbouring masses. Newton's second law and Hooke's law can be directly applied on the masses to work out the position of each mass in the next step rather than interpolating the points along the elements between two nodes and using shape functions to predict the deformed shape of the element which is carried out in FEM [20].

2.1 Surface modelling and assumptions

As shown in Fig. 2(a), a three-dimensional, 2-layer lattice of lumped masses was developed in which the masses are interconnected together through linear springs and dampers. To clarify the connections of this 3D mass-spring-damper network, one corner of the surface has been magnified in Fig. 2(b).

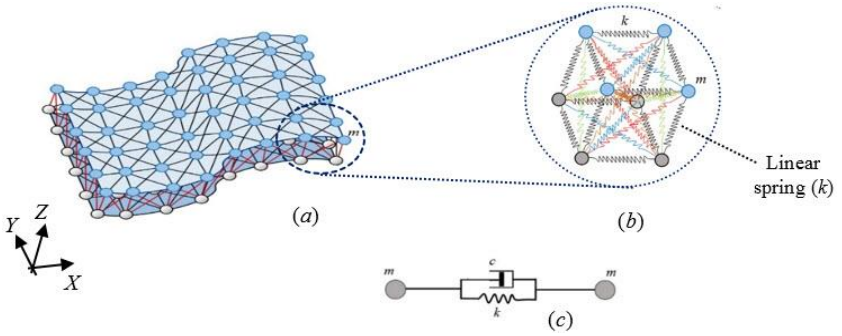

Fig. 2. Representation of the developed lumped-mass models; a) 2-layer LDCS model, b) close-up view of one corner of the surface model composed of 8 masses interconnected by liner springs, c) The featured spring-damper link connecting every two masses in the model

Because of the large surface deformations expected in LDCS, the planes of the surface that are perpendicular to the neutral plane at rest do not remain perpendicular after deformation. Therefore, the model includes diagonal springs in all available directions to enable shear effects to be considered and thus imply a more realistic behaviour of the actuated surface. As a result of this configuration a typical mass in the middle of one of the two layers is linked with 8 surrounding masses in the same layer along with 9 masses located on the opposite layer of the model. So a mass in the middle of one plane as shown in Fig. 3 is surrounded by 17 masses in total while the masses placed on surface edges and corners are linked to fewer of masses, i.e. 11 and 7 respectively. In this article any spring link is collocated with a damper of damping coefficient c as shown in Fig. 2(c), however these are not depicted in the figures for clarity. The dampers are influential in providing the rate of energy absorption and suppression of the oscillations caused by loading and deformation of the surface.

The dynamics of a mass in the model is yielded by its own weight in combination with the forces exerted by surrounding springs. Moreover, some masses might be in contact with ambient systems that are then subject to external loading such as the interactive forces and moments applied directly by the actuators integrated with the surface. The model developed in this work contains few simplifying assumptions. The surface is not constrained in a particular axis. The velocity and acceleration of the masses are taken into account in all spatial Cartesian coordinates. As one of the main assumptions in this model, torsional springs have been neglected to be applied around the masses to avoid extremely added run time for solving the equations of motion related to angular momentum. This solution has been previously applied for modeling planar flexible mechanical systems such as 2D, beam-like arrays [15]. Instead, to provide shear effects, every mass is diagonally linked to the all surrounding masses which means a lumped mass in the middle of the surface (and not located on the edge) is interconnected with 12 masses only through diagonally positioned springs (see Fig. 3). As a result, the in-depth thickness can be applied to thicker surfaces. Also the surface model is flat and its main axes are straight before loading. Moreover, the material of the model in this work is assumed elastic, homogenous and isotropic.

2.2 Governing equations

The overall dynamics of the 3D grid are given by the following equation which consists of matrix terms pertinent to all the existing masses

$$[M]\{\ddot{U}\} + [C]\{\dot{U}\} + [K]\{U\} = F(t) \qquad (1)$$

where U stands for the vector of displacement, $[M]$ the inconsistent or diagonal lumped mass matrix, $[C]$ the damping matrix, $[K]$ the stiffness matrix, and $F(t)$ is the vector representing external forces (F_{ext}) and gravity (W) acting on the model i.e.

$$F(t)=F_{ext}+W \qquad (2)$$

The spring force F_q caused by the transition of every two connected masses, according to Hooke's law, is determined as the following

$$F_q = k_q u_q^{12} + c_q \dot{u}_q^{12} \qquad (3)$$

where q represents $\hat{q} = \hat{i}, \hat{j}, \hat{k}$ which are unit vectors for the Cartesian coordinates X, Y, and Z respectively. Likewise k_q and c_q are the stiffness of the spring and damping coefficient in direction q respectively, and u_q^{12} stands for the net stretch or compression of the spring along the coordinate q occurred after deformation which is determined through the following equation

$$u_q^{12} = \left[\left((l_x + u_{2x} - u_{1x})^2 + (l_y + u_{2y} - u_{1y})^2 + (l_z + u_{2z} - u_{1z})^2\right)^{1/2} - L\right] \times \left[\frac{(l_q + u_{2q} - u_{1q})}{\left((l_x + u_{2x} - u_{1x})^2 + (l_y + u_{2y} - u_{1y})^2 + (l_z + u_{2z} - u_{1z})^2\right)^{1/2}}\right] \qquad (4)$$

Moreover $\dot{u}_q^{12}$ in (3) is the time derivative of (4) defined as $\dot{u}_q^{12} = \frac{d}{dt}(u_q^{12})$. The parameter u_{iq} (i =1, 2 and q= x, y, z) in (4) is the component of vector U in (1). Also, l_q stands for the distance between two masses in the direction q. Then a set of equations whose number depends on the number of lumped masses multiplied by 3 (the number of coordinates), can be solved numerically in parallel. Therefore, for the 2-layer grid of 9x9 lumped masses developed in this work, a mass matrix of 492x492 and a displacement vector of 492 components were built up accordingly to be solved numerically. The average simulation runtime for this set of equations was 225 seconds. All the equations of motion and numerical simulation were implemented using the commercial software MATLAB R2016a.

Fig. 3 shows how a mass located in the center of one of the two surface's layer is bound to other masses by 17 linear springs.

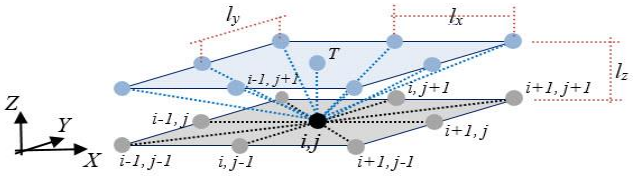

Fig. 3. Geometrical arrangement of the point masses connecting to the typical central mass *i,j* in the two-layer surface model

In this illustration the surrounding masses are indexed by *i,j* abbreviations to identify positions and directions. Also, the index *T* stands for the masses located in the top layer. The equations of motion for the central point is then given by

$$
\begin{aligned}
u_q^{i,j} = \int_{t_1}^{t_2}\left(\int_{t_1}^{t_2} \ddot{u}_q^{i,j}\, dt\right)dt \\
= \frac{1}{m}\int_{t_1}^{t_2}\Big(\int_{t_1}^{t_2}\sum F_q(t)dt\Big)dt = \frac{1}{m}\int_{t_1}^{t_2}\Big(\int_{t_1}^{t_2}\{k_{aq}\left[u_q^{i-1,j}\right. \\
\left. + u_q^{i+1,j} + u_q^{i,j+1} + u_q^{i,j-1}\right] \\
+ k_{dq}\left[u_q^{i+1,j+1} + u_q^{i+1,j-1} + u_q^{i-1,j+1} + u_q^{i-1,j-1}\right] \\
+ k_{dq}^{T}\left[u_q^{(i-1,j)_T} + u_q^{(i+1,j)_T} + u_q^{(i,j+1)_T} + u_q^{(i,j-1)_T}\right] \\
+ k_{ddq}^{T}\left[u_q^{(i+1,j+1)_T} + u_q^{(i+1,j-1)_T} + u_q^{(i-1,j+1)_T} + u_q^{(i-1,j-1)_T}\right] \\
+ k_{zq}u_q^{(i,j)_T} \\
+ c_z\frac{d}{dt}\left[u_q^{i-1,j} + u_q^{i+1,j} + u_q^{i,j+1} + u_q^{i,j-1} + u_q^{i+1,j+1}\right. \\
+ u_q^{i+1,j-1} + u_q^{i-1,j+1} + u_q^{i-1,j-1} + u_q^{(i-1,j)_T} + u_q^{(i+1,j)_T} \\
+ u_q^{(i,j+1)_T} + u_q^{(i,j-1)_T} + u_q^{(i+1,j+1)_T} + u_q^{(i+1,j-1)_T} + u_q^{(i-1,j+1)_T} \\
\left. + u_q^{(i-1,j-1)_T} + u_q^{(i,j)_T}\right] + F_{(ext)q} - W\}dt\Big)dt
\end{aligned}
\tag{5}
$$

where the terms u_q, (q = x, y, z) for the masses in all positions except the central mass (*i,j*) are determined using (4) noting that all the parameters l_x, l_y, l_z, and L can be given different values depending on the position of each mass relative to the mass *i,j*. In the current work, the assumption considered for the mass grid is $l_x = l_y = l$ while the thickness l_z can be quantified independently. Also, the spring stiffness varies in different directions depending on the positioning status of the springs. Accordingly, k_{aq} for $q = x, y, z$ in (5) stands for the stiffness of the *axial* springs in the planar layers in the direction q with the unloaded spring length of L= l and k_{dq} represents the stiffness of *diagonal* springs in plane with the unloaded length $L = \sqrt{2}l$. Likewise k_{dq}^{T} denotes the stiffness of the diagonal springs between the bottom and top layers with $L = \sqrt{{l_z}^2 + l^2}$; k_{ddq}^{T} the diagonal springs between the two layers but with the furthest distance of $L = \sqrt{{l_z}^2 + 2l^2}$; and finally k_{zq} is the stiffness of the spring

connecting the mass (i,j) to $(i,j)_T$ with the unloaded length $L = l_z$. Any external forces in the model (e.g. those applied by actuators and gravity effects) are taken into account by $F_{(ext)q}$ and W respectively with the gravity force applied in the z-direction. Note that the terms corresponding to damping forces vanish in steady-state conditions and they affect the displacements only in transition states.

The equations for the masses located at the top layer are similar to (5) where the places of the top and bottom layers are swapped. Here the index T is replaced by B which indicates the masses located in the bottom layer of the model.

It should be noted that the equations of motion for boundary masses are different based on imposed conditions. When a mass is constrained in specific directions, the corresponding displacements must become zero rather than being calculated through (4). Likewise, for the masses linked to actuators, the amount of displacement is initially dictated by the motion of an actuator to which the mass is bound. In this case, some u_q terms in the far-right side of (5) is replaced by the displacements of corresponding points of the actuator.

3 Experimental test rig setup

To validate the model for its application to LDCS, several statically deformed surface samples were constructed and their displacements were measured for comparison with the model. From these results, a suitable Young's modulus for the surface was determined through simple tensile tests. Then the experimental and lumped mass model results were compared for each test sample.

In the current paper two surface configurations are presented. Fig. 4 depicts these two samples in the test setup; one with two clamped edges of zero curvature (Fig. 4*a*) and the other a sample with one clamped edge consisting of a steel rod which has been bent to the curvature 4.0 m^{-1} to represent the displacement of an actuator (Fig. 4*b*). Indicated in Fig. **4** are also the four points P_1, P_2, P_3, and P_4 whose displacements will be measured to be compared with modelling results. Point P_1 is located in the centre of the square surface, points P_2 and P_3 are on the middle of two sides of the surface and point P_4 is on its farthest corner.

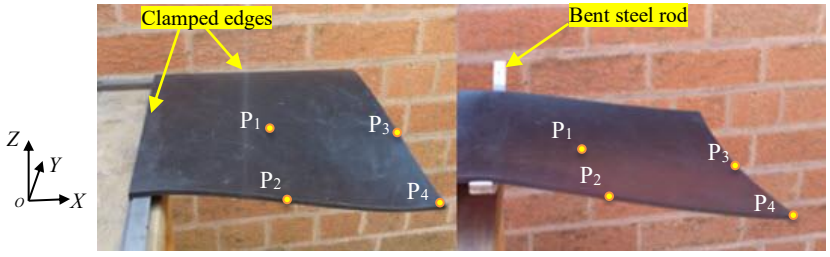

(*a*) : test 1 (*b*) : test 2

Fig. 4. Pictures of two test surface configurations; *a*): Test 1- Surface of two perpendicular clamped edges with no curvature *b*): Test 2- surface with one clamped edge bent by an actuator to the curvature 4.0 m^{-1}

Both flexible surfaces shown in Fig. 4 were cut in square shapes with the size of 0.188 *m* for each side. They were manufactured from a roll of nitrile rubber sheet of thickness 3 mm. The density of the rubber was found to be 1678 kg/m^3 by measuring the mass and volume of several samples. For Poisson's ratio, a typical value of 0.48 for rubber was used. The tensile test to approximate Young's modulus was carried out on different sized rubber samples. This was done using an empirical approach based on maximum deflection of the rubber samples compared with the data produced by the surface model. A mean Young's modulus was eventually concluded as E=0.0545 GPa.

To minimize the residual curvature of the rubber from storage on a roll, the surfaces were stacked and a 10kg weight was placed on top for 48 hours prior to assembly. Once bent the steel rod actuators were securely fixed to the rubber surface using double sided acrylic foam tape. To determine the displacement of desired points on the surface, *fringe projection techniques* were selected. A typical fringe projection system consists of a projection unit, a camera and a processing/analysis unit. The system used in the current study was composed of a laptop connected to a multimedia LCD projector, with a converging lens of 10 cm focal length, along with a PixeLINK PL-A741 CCD camera with a resolution of 1280x1024 pixels in grayscale. This method has been extensively investigated in the past and a summary of the technique with further details can be found in a review by Gorthi and Rastoghi [21]. The key advantage of this method is that it is non-contact and consequently the surface samples are not affected during measurement while high resolution 3D data for the points of interest are gathered almost instantaneously with measuring displacements up to 0.01 mm. A diagram of the setup used for our experiment is shown in Fig. 5.

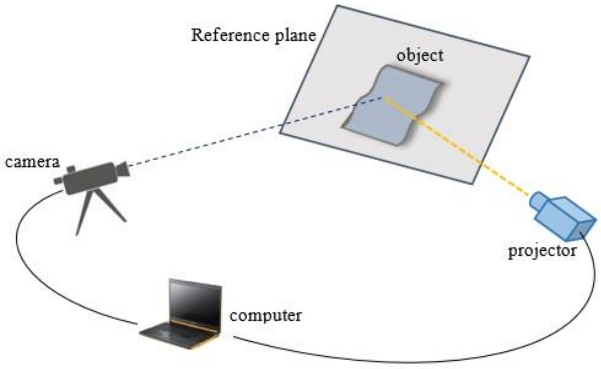

Fig. 5. Setup for Fringe Projection Techniques

4 Comparison of modelling and experimental results

4.1 Static Displacements

The first step in comparing the results was to initialise running the model within the solver with the material properties, surface parameters and boundary conditions for each test. Also the model coordinate system was adjusted according to the experimental test configurations. The surface model contains a 2-layer grid of 9x9 masses in each layer configured in the

way described in Section 2. Therefore 162 masses of m=0.0011 kg were utilised to build up the surface model and to conform to the experimental test surfaces. To approximate the spring constants of the LDCS model, an approach presented in [15], developed for lumped-mass systems, was utilised which worked out an average value of k=550N/m for the set of spring constants to match the experimentally determined Young's modulus.

For test 1 shown in Fig. 4*a* with two clamped straight edges, no actuator was needed for the surface model. For this reason, the masses on these two edges were simply constrained in all directions and the rest of the model was exposed to gravity force acting on each mass. In contrast, to implement test 2, an actuator model was required to deform the single clamped edge of the surface with the curvature 4.0 m^{-1} according to the curved surface in the test. Hence an actuator model was developed that matches the physical configuration of the surface model along that edge. The actuator was also modelled as a multi-body system with lumped segments of given mass and moment of inertia values linked by torsional springs and dampers developed through a Lagrangian formulation and set to approximate the desired curvature. The actuator was then integrated to the surface model to create any curvature of interest in the surface. In this way, the surface model is shown to be decoupled from the actuator model with only force interaction points required should other actuation models be employed. This also enables other actuation configurations to be easily applied when modelling LDCS.

For both tests the lumped-mass models were then loaded under their own weight to present the preliminary dynamic performance of the approach and to evaluate their consistency with the surface undergoing large deflections. Fig. 6 presents the results of the modelled surfaces for test 1 and test 2. The displacements of the four points of the surfaces indicated in Fig. 4 and Fig. 6 have been compared in Table 1 and Table 2 for test 1 and test 2 respectively. Table 3 presents a summary of the error between the experiment and simulation results for the given points.

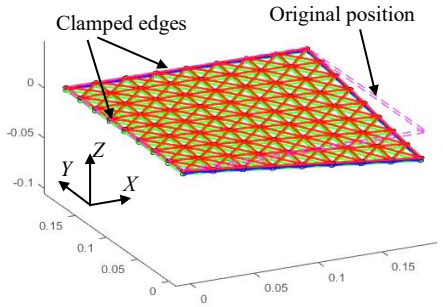

a): test 1- Straight clamped edges

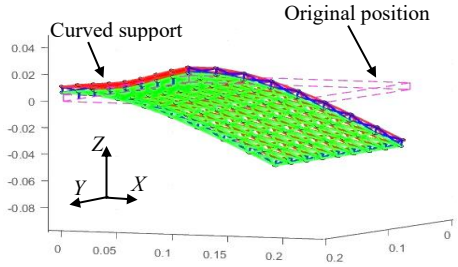

b): test 2 – Curved support on one edge

Fig. 6. Representation of lumped mass models under gravity for comparison with the experimental test surfaces shown in Fig. 4

Table 1. Comparison of the displacement results of the lumped mass model for a LDCS (Fig. 6a) with the experimental test 1 (Fig. 4a) at four different points of the surface. Data are in [mm].

Displacement (m)		**P$_1$**	**P$_2$**	**P$_3$**	**P$_4$**
Modelling	u_x	-0.33	-0.87	-0.76	-1.80
	u_y	0.33	0.76	0.87	1.80
	u_z	-6.02	-13.43	-13.43	-18.17
Experimental	u_x	-0.35	-0.81	-0.71	-1.91
	u_y	0.34	0.72	0.82	-1.86
	u_z	-6.45	-14.33	-14.33	-20.09

Table 2. Comparison of the displacement results of the lumped mass model for a LDCS (Fig. 6*b*) with the experimental test 2 (Fig. 4*b*) at four different points of the surface. Data are in [mm].

Displacement (m)		**P$_1$**	**P$_2$**	**P$_3$**	**P$_4$**
Modelling	u_x	-8.33	-8.01	-21.85	-20.48
	u_y	0.00	-0.05	0.00	-0.12
	u_z	-19.35	-14.29	-41.54	-31.34
Experimental	u_x	-7.94	-7.66	-20.75	-19.39
	u_y	0.00	-0.05	0.00	-0.11
	u_z	-18.87	-13.77	-38.88	-28.95

Table 3. Summary of error between modelling and experimental results at four points of the surface for both test 1 and test 2.

% Error		P_1	P_2	P_3	P_4
Test 1	u_x	5.7	6.8	6.5	5.7
	u_y	2.9	5.2	5.7	3.2
	u_z	6.6	6.3	6.3	9.6
Test 2	u_x	4.6	4.3	5	5.3
	u_y	0	0	0	8.3
	u_z	2.4	3.6	6.4	7.6

General comparison between the model and experimental results presented in the tables reveals that the model successfully generated surfaces with comparable shapes for both tests 1 and 2. Carefully investigation of the modelling results identify the internal consistency of the model. For example, from the results of test 1 shown in Table 1, it is seen that as expected $|u_{x(P2)}| = -|u_{y(P3)}|$, $|u_{y(P2)}| = -|u_{x(P3)}|$ and $|u_{z(P2)}| = |u_{z(P3)}|$ which are intuitively rational based on the symmetry of boundary conditions and loading for the surface. Likewise, according to the results of test 2 shown in Table 2, the points P_1 and P_3 are not displaced at all in the *y*-direction which is expected due to the symmetry about the surface's central *x*-axis. As seen in Table 3, the point P_4 in test 1 undergoes the most notable difference in the Table but does not exceed 10% with mean percentage error of 4.8%. These errors are due to several factors including failure to remove all residual curvature from the rubber before assembly. This is roughly apparent in Fig. 4*a* where there is a minor unwanted twist in the experimental surface compared to the model. Another source of error is that because the surfaces were assembled by hand, the steel rods were not in the exact modelled position. This creates error in the surface shape which would be picked up in measurements, but not be present in the idealized model.

As with all other discretization techniques, the more nodes (here 'lumped masses') considered in the developed model, the more accurate the results achievable. But, on the other hand, the time consumed to construct the model as well as the computational burden to solve the problem will be increased. As a result, future work will need to consider the relative trade-offs between accuracy and computational cost. Overall, however these results indicate a reliable conformity despite the limited number of masses used in the model with a mean percentage error of 4.8% and relative resulting shapes remaining the same.

4.2 Dynamic Analysis

It should be noted that in the videos the surface model was run from zero gravity at the very beginning. For this reason, gravity switches abruptly from g=0 to g=9.81 m/s^2 after runtime starts, which causes the surface to undergo oscillation over time until it settles down at the final deflected position. This arrangement was programmed intentionally to simulate the dynamic behaviour of a soft surface when it is suddenly exposed to external forces such as gravity. However, this was not recorded in the experiments here and is the subject of future work. The magnitude of this oscillation can be managed by changing the material damping properties considered in the model. As an example of this however, Fig. 7 **Error! Reference source not found.**shows the displacement of point P_4 in test 1 in the three directions *x*, *y* and *z*.

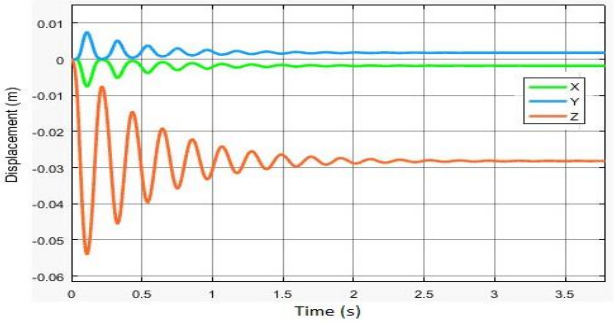

Fig. 7. Displacements of point P_4 on the surface in test 1 over time

5 Concluding remarks and future work

In this work the application of a lumped mass approach to model 3D actuated Large Displacement Continuum Surfaces (LDCS) composed of mass-spring-damper arrays was presented. The developed model enables representation of behaviour of arbitrarily thick flexible plates to encompass in-depth and transverse shear effects. The model is also adaptable for integration with a variety of actuation elements to bend the surface into various curvatures.

A test rig was set up and two experimental surface configurations were tested as part of initial validation efforts. The configurations showed satisfactory agreement between the experimental and model results for such a flexible surface undergoing uniformly distributed gravitational loads. The mean percentage error was found to be 4.8%, while the results matched the expected performance.

Given the promising results obtained here for both LDCS configurations, further research to improve the model is motivated and ongoing. For example, new materials to form the LDCS are being evaluated and tested to see if one could overcome the material issues encountered here while matching the assumptions made in the current model. Additionally, ongoing work will extend the 3D lumped surface model integrated with the actuator models to deliver a robust dynamic model for actuated LDCS that will precisely describe the surface profile for both displacement of any point across the surface, as well as interactive forces applied by actuators and external forces in a range of configurations. Further, experiments will be carried out on multiple actuator configurations, where the motion of the flexible surface is constrained by additional, more complex boundary conditions. This will enable into a longer term research looking to develop accurate and efficient control of actuated continuum surfaces undergoing large deformations.

Acknowledgement

This work is funded and supported by the Engineering and Physical Sciences Research Council (EPSRC) under grant number: EP/N022505/1, and the Natural Science Foundation of China (NSFC) under grant number: 51611130202.

References

1. Burgner-Kahrs, J., Rucker, D.C., Choset, H.: "Continuum Robots for Medical Applications: A Survey," *IEEE Transactions on Robotics,* vol. 31, no. 6, pp. 1261-1280, 2015.
2. Santiago, J.L.C., Walker, I.D., and Godage, I.S.: "Continuum robots for space applications based on layer-jamming scales with stiffening capability," in *IEEE Aerospace Conference*, 2015: 1-13.
3. Bajo A., Simaan, N.: "Finding lost wrenches: using continuum robots for contact detection and estimation of contact location," in *IEEE International Conference on Robotics and Automation*, pp. 3666-3673, Anchorage, Alaska, 2010.
4. Walker, I.D.: "Continuous Backbone "Continuum" Robot Manipulators," *ISRN Robotics,* vol. 2013, pp. 1-19, 2013.
5. Godage, I.S., Medrano-Cerda, G.A., Branson, D.T., Guglielmino, E., Caldwell D.G.: "Dynamics for Variable Length Multisection Continuum Arms," *The International Journal of Robotics Research,* vol. 35, no. 6, pp. 695-772, 2016.
6. Conrad, B.L., Jung, J., Penning, R.S.: "Interleaved continuum-rigid manipulation: An augmented approach for robotic minimally-invasive flexible catheter-based procedures," *IEEE International Conference on Robotics and Automation,* pp. 718-724, 2013.
7. Webster, R.J., Jones, B.A., "Design and Kinematic Modeling of Constant Curvature Continuum Robots: A Review," *The International Journal of Robotics Research,* vol. 29, no. 13, pp. 1661-1683, 2010.
8. Tatlicioglu, E., Walker I.D., Dawson, D.M.: "Dynamic Modelling for Planar Extensible Continuum Robot Manipulators," in *IEEE International Conference on Robotics and Automation,*, pp. 1357-1362, Roma, 2007.
9. Bailly, Y., Amirat, Y., Fried, G.: "Modeling and Control of a Continuum Style Microrobot for Endovascular Surgery," *IEEE Transactions on Robotics,* vol. 27, no. 5, pp. 1024-1030, 2011.
10. Kano, T., Watanabe, Y., Ishiguro, A.: "Sheetbot, Two-dimensional sheet-like robot as a tool for constructing universal decentralized control systems," in *IEEE International Conference on Robotics and Automation (ICRA)*, 2012: 3733-3738.
11. Medina O., Shapiro A., Shvalb, N.: "Minimal Actuation for a Flat Actuated Flexible Manifold," *IEEE Transactions on Robotics,* vol. 32, no. 3, pp. 698-706, 2016.
12. Merino, J., Threatt, A.L., Walker I.D., Green, K.E.: "Forward Kinematic Model for Continuum Robotic Surfaces," in *IEEE/RSJ International Conference on Intelligent Robots and Systems (IROS)*, pp. 3453-3460, Vilamoura, Algarve, Portugal, 2012.
13. James H. Jr. Williams, Fundamental of applied dynamics, USA: John Wiley & Sons, 1996.
14. Mesit, J., Guha, R., Chaudhry, S.: "3D Soft Body Simulation Using Mass-spring System with Internal Pressure Force and Simplified Implicit Integration," *Journal of computers,* vol. 2, no. 8, pp. 34-43, October 2007.
15. Habibi H., O'Connor, W.: "Wave-based control of planar motion of beam-like mass–spring arrays," *Wave Motion,* vol. 72, p. 317–330, 2017.
16. Liu, T., Bargteil, A.W., O'Brien, J.F., Kavan, L., "Fast simulation of mass-spring systems," *ACM Transactions on Graphics,* vol. 32, no. 6, pp. 1-7, 2013.

17. Anthonis, J., Ramon, H., “Comparison between the discrete and finite element methods for modelling an agricultural spray boom - Part 1: Theoretical derivation,” *Journal of Sound and Vibration,* vol. 266, p. 515–534, 2003.

18. Kino, M., Murakami, T., Ohnishi, K.: “A vibration suppression and disturbance rejection strategy of flexible manipulator by multiple acceleration feedback,” in *Proceedings of Movic ’98, Vol. 2, pp. 781–786*, Zurich, 1998.

19. Torfs, D.E., Vuerinckx, R., Swevers, J., and Schoukens J., “Comparison of two feedforward design methods aiming at accurate trajectory tracking of the endpoint of a flexible robot arm,” *IEEE Transactions on Control Systems Technology,* vol. 6, no. 1, pp. 2-14, 1998.

20. Petyt, M.: Introduction to Finite Element Vibration Analysis, Cambridge: Cambridge University Press, 1990.

21. Gorthi, S.S., Rastogi, P.: “Fringe Projection Techniques: Whither we are?,” *Optics and Lasers in Engineering,* vol. 48, no. 2, pp. 133-140, 2010.